

High efficiency TOPCon solar cells with micron/nano-structured emitter for a balance of light-trapping and surface passivation

Jiahui Xu ^{a,b}, Cheng Chen ^b, Cui Liu ^{a,*}, Jia Chen ^b, Zhifeng Liu ^b, Xiao Yuan ^a, Hongbo Li ^{a, **}

^a School of Materials Science and Engineering, East China University of Science and Technology, Shanghai, 200237, China

^b Jolywood (Taizhou) Solar Technology Co., Ltd, Taizhou, Jiangsu, 225500, China



ARTICLE INFO

Keywords:
TOPCon
Nanopores
Light-trapping
Wide-angle
Surface passivation

ABSTRACT

At present, conventional micron-pyramid texture is imperfect for further reducing optical reflection loss and improving photoelectric conversion efficiency (PCE) of tunnel oxide passivating contact (TOPCon) solar cells. Herein, reactive ion etching technique is used to fabricate nanopores on top of pre-formed micron-pyramid silicon surface, called NPP structure. The equivalent medium layer with graded refractive index appeared on NPP textures makes the absorption of almost all incident light independent of the wavelength and angle. However, serious Auger recombination and surface recombination associated with NPP structure is detrimental to emitter passivation, usually counteracting the photocurrent gain. To identify an appropriate balance of light-trapping and surface passivation, we investigate the impact of different radio-frequency power (P_{RF}) on the optical and electrical properties of TOPCon solar cells and discusses the underlying structural causes behind these observed improvements. Finally, we demonstrate NPP TOPCon solar cells with an average short-circuit current density of 41.44 mA/cm^2 and an average PCE of 23.55% at the P_{RF} of 600 W. Besides, the external quantum efficiency results under various incident angles from 0° to 70° exhibited excellent wide-angle spectral absorption capability, which is significant for solar cells working in an outdoor environment.

1. Introduction

Over the past few years, the industrial-level bifacial tunnel oxide passivating contact (TOPCon) solar cells have demonstrated an impressive development speed, with photoelectric conversion efficiency (PCE) exceeding 24.5% [1]. Moreover, TOPCon solar cells allow a compatibility with mainstream passivated emitter and rear solar cells (PERC) mass production, and a maximum theoretical PCE up to 28.7%, which are promising as an alternative to next-generation solar cell technology [2]. Unfortunately, the front-side optical reflection loss still accounts for a large portion of power loss for bifacial TOPCon solar cells, caused by conventional micron-pyramid texture with poor short-wavelength absorption [3,4]. Hence, researchers put forward and developed various advanced light-trapping textures to enhance the utilization of the available solar spectrum and obtain a high photocurrent density (J_{ph}) [5,6]. Nanostructured silicon texture, also known as “black silicon (b-Si)”, due to superior antireflection capability, is considered a powerful approach for improving J_{ph} , and has been widely studied in many fields, such as photodetectors [7,8], biological monitors [9]. In

addition, b-Si textures maintain an effective reflection elimination over a wide range of incident angles (θ) [10–12], which is significant for evaluating the power generation benefits of solar cells under constantly changing sun angle. Many attempts have been made to integrate b-Si textures with various solar cells, such as the traditional aluminum back surface field solar cells, PERC, or interdigitated back-contact back-junction (IBC) solar cells [3,13–15].

In general, b-Si textures can be formed by various techniques, including laser texturing [16,17], reactive ion etching (RIE) [18,19], and metal-catalyzed chemical etching (MCCE) [13,20,21]. Among those, RIE technique is more suitable for creating b-Si textures in industrial solar cell production because of large-scale preparation, rapid reaction, and no noble metal pollution [22–25]. Until now there have been some laboratory-grade attempts on n-type silicon solar cells based RIE technique. For example, Savin et al. [19] fabricated a nanopillar surface using RIE in IBC solar cells with a short-circuit density (J_{sc}) of 42.2 mA/cm^2 and a relative J_{sc} loss of less than 1% at the θ of 60° in comparison to the normal incidence ($\theta = 0^\circ$). To inhibit emitter recombination of b-Si prepared by RIE, G. von Gastrow et al. [26]

* Corresponding author.

** Corresponding author.

E-mail addresses: liucui@ecust.edu.cn (C. Liu), lihongbo@ecust.edu.cn (H. Li).

passivated the implanted b-Si emitter with atomic layer deposited (ALD) aluminum oxide (Al_2O_3) layer, yielding an emitter saturation current density (J_{0e}) of 20 fA/cm^2 . However, there is little information about the integration of RIE b-Si textures with n-type industrial TOPCon solar cells.

In this work, we have successfully developed the RIE b-Si technique for high-efficient n-type bifacial TOPCon solar cells in existing industrial production lines. Here, the nano/micron-composite textures were formed by a texture-on-texture approach. In other words, the RIE technique uniformly creates nanopores on top of a pre-formed alkaline etched micron-pyramid surface, named as NPP structure. Specifically, the impacts of different RIE radio-frequency power (P_{RF}) on the photovoltaic properties of NPP TOPCon solar cells were systematically investigated. Meanwhile, an optimized boron diffusion process and a high-quality passivation stack of ALD- Al_2O_3 /plasma-enhanced chemical vapor deposition (PECVD) silicon nitride (SiN_x) layer were discussed and used to keep the balance of light-trapping and surface passivation. As a result, the industrial large-scale NPP TOPCon solar cells at the P_{RF} of 600 W exhibit high performance with an average J_{sc} of 41.44 mA/cm^2 and an average PCE of 23.55%. In addition, we demonstrated the wide-angle power generation capability of NPP TOPCon solar cells, with the J_{sc} loss under 4.5% for the θ below 70° . This paper provides a reference for the application of RIE b-Si technique in industrial n-type bifacial TOPCon solar cells.

2. Experimental

2.1. Surface textures

For NPP TOPCon solar cells, n-type Czochralski (CZ) silicon wafers with $158.75 \times 158.75 \text{ mm}^2$ size, (100) grain orientation, 1–3 Ωcm -resistivity, and 170 μm -thickness were applied as substrates. Different from pure b-Si textures prepared from a planar silicon wafer, the first step in this process was immersing the silicon wafers after a standard RCA cleaning in a mixture of 1.2 wt% sodium hydroxide (NaOH) and 6 wt% isopropyl alcohol (IPA) at 82°C for 20 min to form a random micron-pyramid surface. Next, a maskless RIE system with a gas mixture of O_2 , Cl_2 and SF_6 was used to prepare packed nanopores on random

micron-pyramid surface. The feature size of NPP structures is regulated and controlled by P_{RF} (100 W, 300 W, 600 W). This P_{RF} parameter was chosen as a variable because it greatly affects the dissociation rate of reactive gases and bombardment kinetic energy of reactive ions, thus impacting the morphology and size [27,28]. The chemical etching mechanisms of this RIE system are explained by Equations (1)–(3) [24, 29,30]:



Fig. 1a delineated the preparation schematic of NPP structures. After that, to remove the plasma-induced damaged layer and round off the sharp silicon structure, the samples were immersed in a buffered oxide etching (BOE) recipe of ammonium fluoride (NH_4F), hydrogen peroxide (H_2O_2), and water (H_2O).

2.2. Fabrication of solar cells

The cross-sectional conceptual diagram of NPP TOPCon solar cells is shown in **Fig. 1b**. In this work, conventional TOPCon solar cells with micron-pyramid texture were set as one reference group, and b-Si TOPCon solar cells with NPP textures at different P_{RF} were set as three test groups. The manufacturing process flow of reference and test TOPCon solar cells is outlined in **Fig. 1c**. The initial quantity of samples per group was 40 silicon wafers. The silicon wafers of test groups have undergone a baseline process of conventional TOPCon solar cells as well as an additional RIE step and a pore-widening process. All silicon wafers were inserted in one graphite boat to form a p-type emitter using boron tribromide source, consisting of a boron trioxide deposition process and a subsequent drive-in process. Then, after etching rear borosilicate glass by HF/HNO_3 mixed solution, a tunnel SiO_x film ($\sim 1.5 \text{ nm}$) and an intrinsic amorphous silicon layer ($\sim 140 \text{ nm}$) were deposited on both sides of silicon wafers in thermal oxidation method and low-pressure chemical vapor deposition (LPCVD) method, respectively. To obtain back-side n-type TOPCon structure, phosphorus dopant was first lead

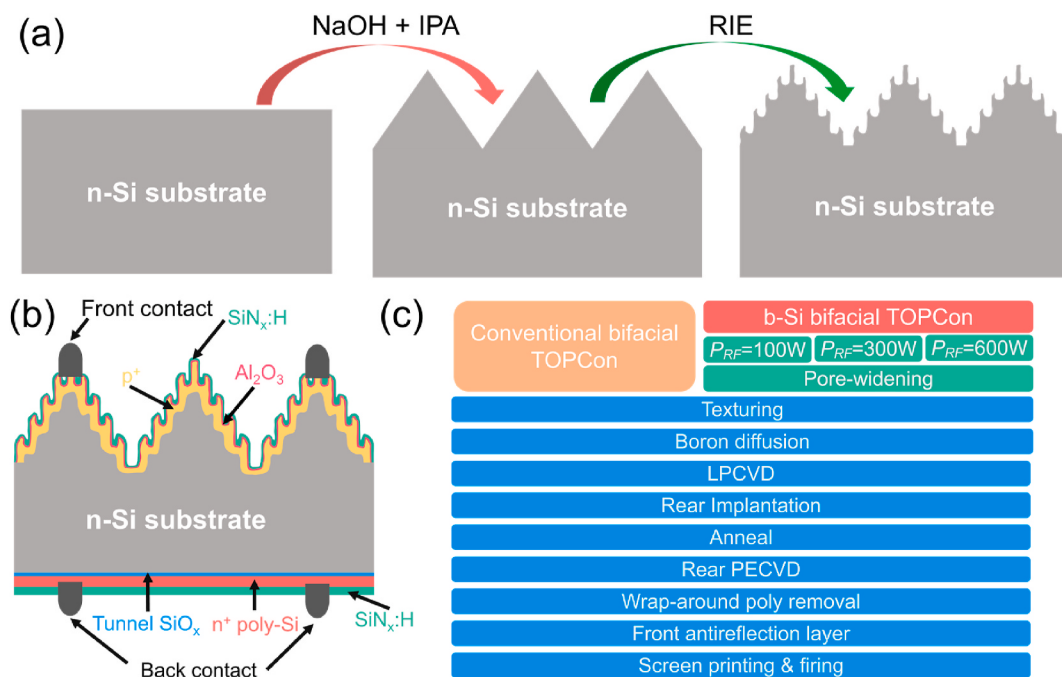


Fig. 1. Design and process of NPP TOPCon solar cells. (a) The preparation schematic for NPP structures. (b) The cross-sectional conceptual diagram of NPP TOPCon solar cells. (c) The manufacturing process flow of reference and test TOPCon solar cells.

into the intrinsic amorphous silicon layer by ion implantation method, and a following 900 °C thermal annealing process was used to activate phosphorus atoms and transform from amorphous to polycrystalline. The n-type polysilicon at the front-side and the wafer edges was removed by HF/HNO₃ mixed solution and a SiN_x layer via PECVD was covered on rear surface to intensify passivation performance. Then, to suppress surface recombination and reflectance loss, the ALD-Al₂O₃ (~4 nm)/PECVD-SiN_x (~75 nm) stacked films were deposited on various texturing emitters. Finally, a metallization pattern with 12 busbars was formed by a screen printing and co-sintered process. It is noteworthy that in view of the extensive number of recombination caused by NPP structures, the boron diffusion process and surface passivation technique were optimized and discussed on baseline process.

2.3. Characterization

Morphologies and feature sizes of NPP structures were characterized using a scanning electron microscope (SEM, SU5000). The reflectance spectra of silicon wafers and solar cells were determined by hemispherical reflectance spectrometry with an integrating sphere from 300 to 1200 nm. The four-probes method was used to measure the sheet resistance (R_{sheet}) of boron doping emitter. The surface concentration distribution of active boron atoms and junction depth (d) were measured by electrochemical capacitance-voltage (ECV, CVP-21) profiling after removing wrap-around polysilicon. To evaluate the passivation performance of different textures, five pieces were randomly selected from each group solar cells before screen printing as lifetime samples. The effective minority carrier lifetime (τ_{eff}), saturation current density (J_0), and implied open-circuit voltage (iV_{oc}) of lifetime samples were extracted from quasi-steady state photoconductance lifetime measurement data (Sinton, WCT-120). Photoluminescence (PL) results of lifetime samples were used to indicate the passivation property and uniformity. External quantum efficiency (EQE) spectra were recognized at a spectral response measurement system. The valuable electrical parameters, including PCE, open-circuit voltage (V_{oc}), J_{sc} , filling factor (FF) and series resistance (R_s), etc., were measured with an in-line, light I-V and Suns- V_{oc} measuring instrument (Sinton, FCT-750).

3. Results and discussions

3.1. Surface morphology and optical property

We fabricated multi-scale NPP structures with three kinds of feature sizes via different P_{RF} . Fig. 2a–c presents the top-view SEM images of NPP surface at 10.0 K magnifications under the P_{RF} of 100 W, 300 W and 600 W, respectively, as well as the corresponding zoom-in SEM images of top view and cross-section view at 30.0 K magnifications. Compared with conventional micron-pyramid texture, the NPP structures reveal a hierarchical surface consisting of dense nanopores on top of random micron-pyramids and nanogrooves between micron-pyramids. According to the SEM image luminance contrast shown in Fig. 2, it is obvious that nanogrooves are deeper and broader than nanopores because the V-shaped intersections between micron-pyramids were subjected to more physical sputtering and chemical etching. Fig. 2 gives clear evidence for different feature sizes under three P_{RF} . Based on SEM results, we count and calculate the simplified geometry parameters of NPP structures at different P_{RF} , including the average nanopore diameter (D), nanogroove width (W), nanogroove projection proportion (C), nanopore depth (D_p) and the enhanced specific surface area ratio ($A_{\text{F}}/A_{\text{proj}}$) [14], as listed in Table 1. Herein, A_{F} represents the front surface area, A_{proj} represents the corresponding projection area.

As shown in Table 1, when the P_{RF} increases from 100 to 600 W, the average width of nanopores increases from 223 to 268 nm, the average width of nanogrooves increases from 360 to 470 nm, and the average depth of nanopores increases from 204 to 277 nm, indicating that wider and deeper nanostructures were formed at higher P_{RF} . This is because

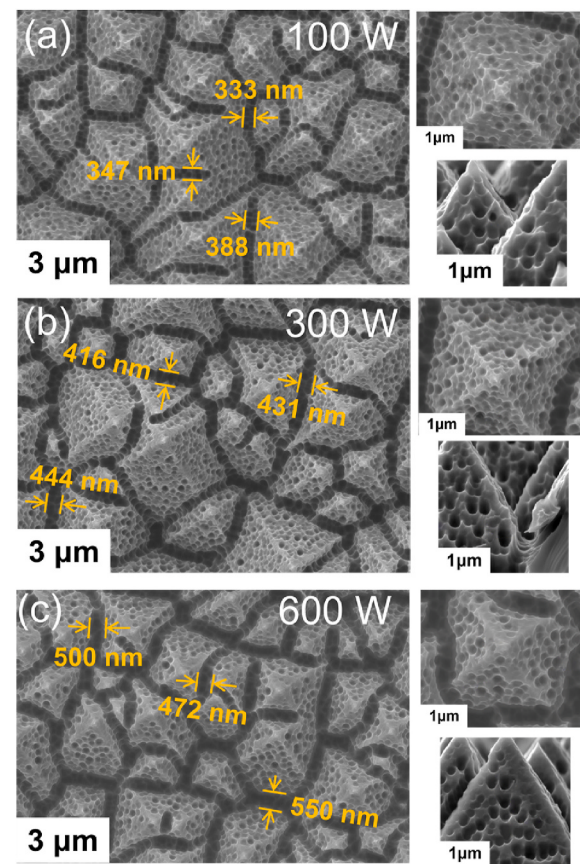


Fig. 2. Top view SEM images of NPP surface morphologies at 10.0 K magnifications (left) as well as the zoom-in SEM images of top view and cross-section view at 30.0 K magnifications (right) under the P_{RF} of (a) 100 W, (b) 300 W and (c) 600 W.

Table 1

Statistical mean structural parameters with the standard deviation of simplified NPP textures at different P_{RF} .

RIE P_{RF} (W)	D (nm)	W (nm)	C (%)	D_p (nm)	$A_{\text{F}}/A_{\text{proj}}$
0 (pyramid)	0	0	0	0	1.79
100	223 ± 18	360 ± 24	17.67 ± 0.28	204 ± 22	4.87
300	240 ± 20	410 ± 29	19.07 ± 0.32	265 ± 22	4.92
600	268 ± 25	470 ± 34	22.23 ± 0.34	277 ± 21	4.82

the increased P_{RF} accelerates the ionization of O₂, Cl₂ and SF₆ as well as physical sputtering of reactive ions and energy-enhanced free electrons [27,31]. Meanwhile, the zoom-in images at cross-section view shown in Fig. 2 indicate that the surface flatness of NPP structures at the P_{RF} of 600 W is smoother than that of 100 W and 300 W, which is likely that the sharp and highly reactive structures formed previously were removed from the surface.

To comprehensively investigate the optical properties of NPP structures at different P_{RF} , we measured the reflectance and transmittance spectra in the wavelength region of 300–1180 nm and calculated the absorptance spectra according to Equation (4), as shown in Fig. 3a–c. Then, the averaged solar spectral values of reflectance (R_{ave}), transmittance (T_{ave}) and absorptance (A_{ave}) were calculated by the following Expression (5) ~ (7) and inserted in Fig. 3, taking conventional micron-pyramid structure as a reference.

$$A(\lambda) = 1 - R(\lambda) - T(\lambda) \quad (4)$$

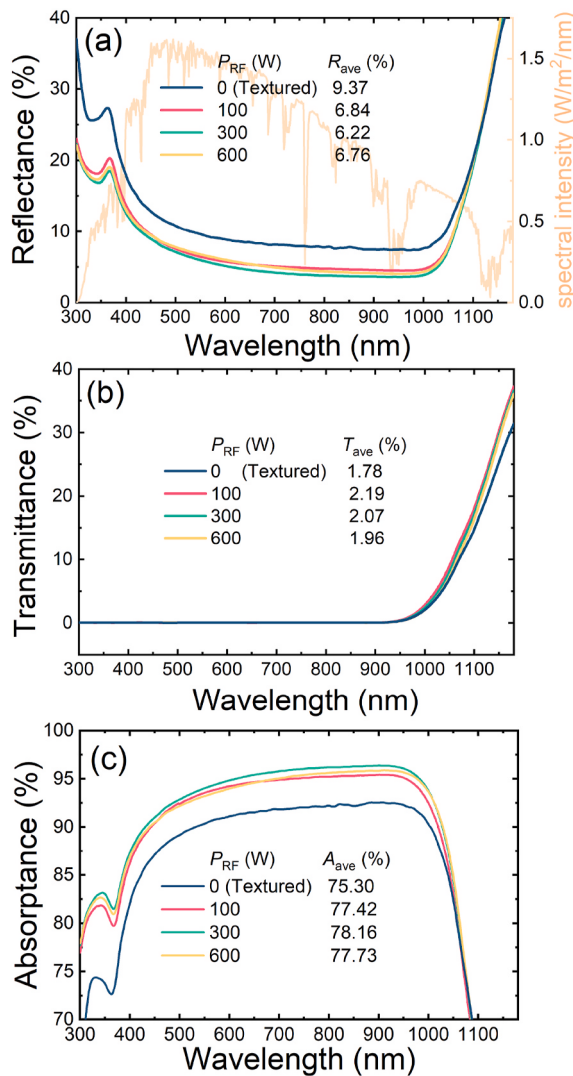


Fig. 3. Evolution of (a) reflectance, (b) transmittance and (c) absorptance spectra of NPP wafers from 300 to 1180 nm at different P_{RF} .

$$R_{ave} = \frac{\int_{300nm}^{1180nm} R(\lambda) \cdot S(\lambda) \cdot d\lambda}{\int_{300nm}^{1180nm} S(\lambda) \cdot d\lambda} \quad (5)$$

$$T_{ave} = \frac{\int_{300nm}^{1180nm} T(\lambda) \cdot S(\lambda) \cdot d\lambda}{\int_{300nm}^{1180nm} S(\lambda) \cdot d\lambda} \quad (6)$$

$$A_{ave} = \frac{\int_{300nm}^{1180nm} A(\lambda) \cdot S(\lambda) \cdot d\lambda}{\int_{300nm}^{1180nm} S(\lambda) \cdot d\lambda} \quad (7)$$

Where $S(\lambda)$ represents the AM1.5 solar spectral response distribution. As shown in Fig. 3a and c, all NPP structures ($R_{ave} \leq 6.84\%$, $A_{ave} \geq 77.4\%$) achieve a notably light-trapping capability over a wide spectral range from 300 to 1050 nm compared to micron-pyramid structure ($R_{ave} \sim 9.37\%$, $A_{ave} \sim 75.3\%$). An equivalent medium layer (EML) with graded refractive index distribution was formed between the air and the silicon substrate [32], because the feature sizes of NPP structures are comparable to or smaller than the incident light wavelength, especially the short-wavelength. The EML effectively enhances light scattering [33], and improves short-wavelength response of silicon wafers in the spectral range of 300–400 nm as shown in Fig. 3a. Meanwhile, the absorptance spectra of NPP structures show a redshift compared with that of micron-pyramid textures, owing to the EML suppressing the strong

reflection originated from the refractive index dispersion effect of silicon substrate [34–36]. Fig. 3b shows that the long-wavelength transmittance of NPP structures is slightly higher than that of micron-pyramid structure due to its thinner wafer thickness after RIE etching and BOE cleaning. Besides, the transmittance of NPP structures at different P_{RF} shows little difference.

According to the structure parameters of NPP textures in Table 1, the increased width of nanopores and nanogrooves at higher P_{RF} reduces the action spectra range of EML, thus, to the detriment of antireflection. Paradoxically, the increased etching depth at higher P_{RF} enhances the reflection times of incident light, beneficial for light-trapping. As shown in Fig. 3c, the R_{ave} of NPP textures decreases from 6.84% to 6.22% when the P_{RF} increases from 100 to 300 W, which indicated that etching depth plays a dominant role in antireflection capability. However, when the P_{RF} increases from 300 to 600 W, the R_{ave} increases from 6.22% to 6.76%. This is because, although etching depth is still increased, the feature size of some nanogrooves is larger than 500 nm, no longer fulfilling the zero-order condition of EML [37].

3.2. Emitter passivation properties

The difficulty of integrating RIE b-Si textures into solar cell production lies in severe Auger recombination and surface Shockley-Read-Hall (SRH) recombination of photo-generated carriers, caused by high surface doping concentration (N_s) and high A^F/A_{proj} of nano-structured surfaces, respectively. In order to suppress Auger recombination, the doping characteristics of NPP emitter based on the P_{RF} of 100 W were investigated and discussed by appropriately adjusting process parameters, including oxygen flow rate, drive-in temperature, and oxidation time during boron diffusion. Fig. 4a shows the ECV curve of NPP emitter with an optimized boron diffusion (OPB) process (red), taking baseline diffusion process on NPP texture (blue) as reference. Compared with NPP emitter with baseline diffusion process ($N_s \sim 5.92 \times 10^{19} \text{ cm}^{-3}$, $d \sim 0.7 \mu\text{m}$), that with OPB process exhibited a reduced N_s peak ($\sim 1.35 \times 10^{19} \text{ cm}^{-3}$) and an increased d length ($\sim 1.26 \mu\text{m}$) because of the internal diffusion of boron atoms in a longer in-situ oxidation time [38]. Fig. 4b compares the average J_0 of NPP cells before screen printing in OPB process ($J_0 \sim 50.4 \text{ fA/cm}^2$) and baseline diffusion process ($J_0 \sim 61.1 \text{ fA/cm}^2$) under the same solar cell manufacturing. For both emitters coated with the same stacked surface passivation layer, the improvement J_0 of NPP cells in OPB process are evidently originated from lessened Auger recombination. Besides, supplement Fig. S1 and Table S1 show the ECV profiles, J_0 and $I-V$ parameters of NPP cells with another boron diffusion process, which is not used as the final boron diffusion process due to higher contact resistivity and lower FF despite exhibiting more excellent J_0 and V_{oc} than the OPB process. Finally, in this paper, the OPB process was applied in all samples at different P_{RF} . Fig. 4c and d shows the ECV curves and R_{sheet} of NPP emitters, respectively, which afford data support to analyze and quantify emitter recombination evolution with different P_{RF} . First, all NPP emitters possess higher N_s , d and lower R_{sheet} than micron-pyramid emitter because NPP emitters with a high A^F/A_{proj} enhance the adsorption and doping of boron atoms in boron diffusion process [3,39]. For NPP emitters formed by RIE, the lower N_s , shallower d and increased R_{sheet} with P_{RF} indicate that larger feature sizes and smoother surface can slightly improve the doping characteristics.

To achieve a high PCE of solar cells, the high-quality surface passivation is critical to prevent unwanted photo-generated carrier recombination occurring on the NPP surface. Supplement Figs. S2–S4 show some attempts on adjusting the passivation technique to find the suitable solution for the nano/micro silicon surface. In this work, the stacked ALD-Al₂O₃/PECVD-SiN_x dielectric layer was finally selected to passivate NPP emitters because it combines excellent chemical passivation with field-effect passivation (negative fixed charge density) on p-type silicon surface [40]. Fig. 5a shows the τ_{eff} as a function of excess carrier density (Δn) for double-sided polished silicon wafers covered

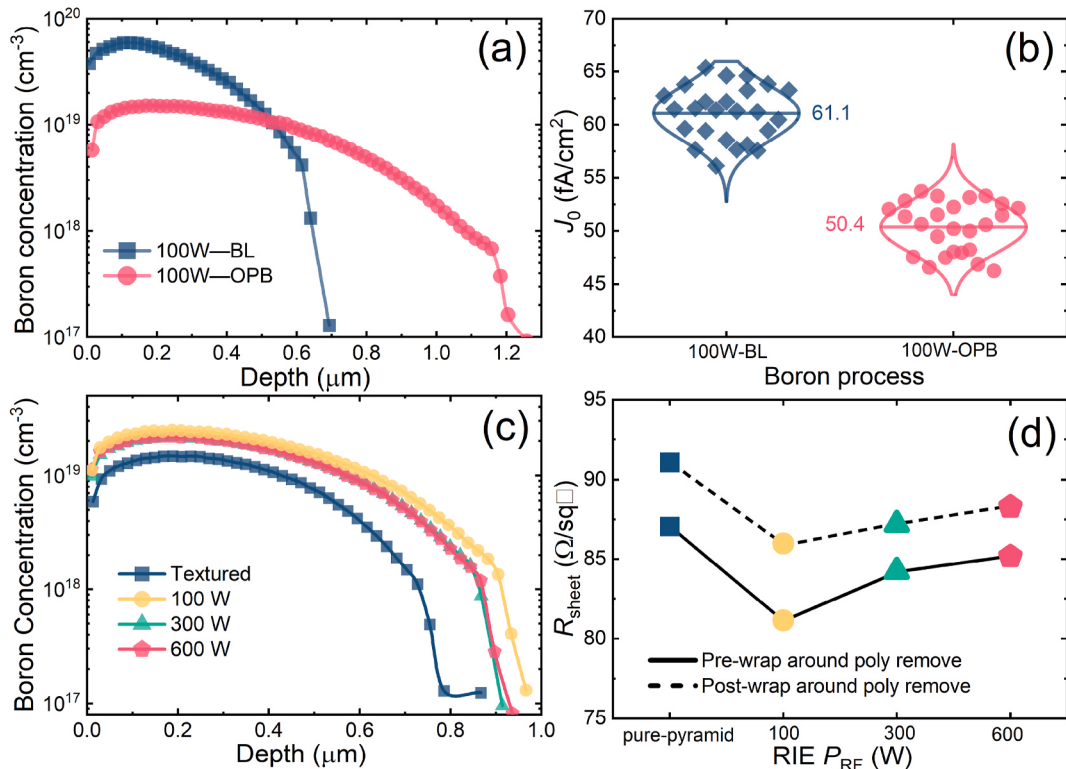


Fig. 4. (a) The ECV profiles and (b) the average J_0 of NPP emitter in OPB process and baseline process at the P_{RF} of 100 W. (c) The ECV profiles of NPP emitters at different P_{RF} . (d) The R_{sheet} of NPP emitters before and after removing around-poly at different P_{RF} . The textured micron-pyramid emitter in the OPB process was taken as a reference.

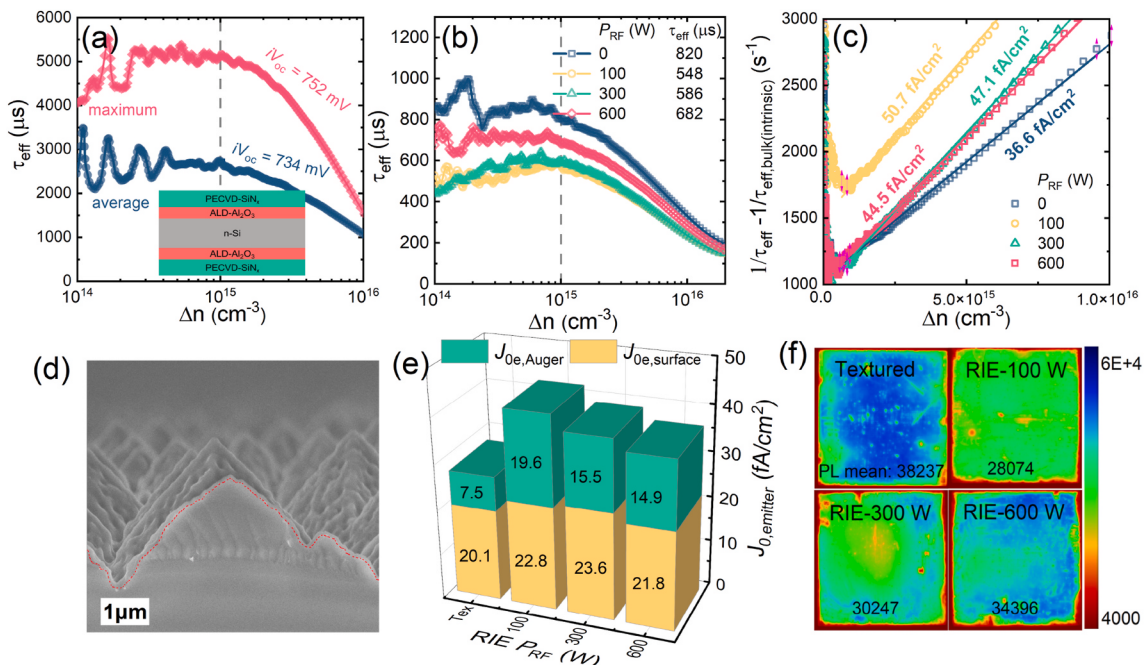


Fig. 5. (a) The τ_{eff} of polished silicon wafers coated with the $\text{Al}_2\text{O}_3/\text{SiN}_x$ stacked layer as a function of Δn . (b) The τ_{eff} and (c) Auger-corrected inverse lifetime comparison of conventional cells and NPP cells before screen printing at different P_{RF} as a function of Δn . The J_0 was extracted from an inverse lifetime with Auger-corrected. (d) The cross-sectional SEM image of NPP cells on front-side. (e) Separated diagram of J_{0e} consisting of $J_{0e, \text{Auger}}$ and $J_{0e, \text{Surface}}$ of conventional cells and NPP cells at different P_{RF} . (f) The relative PL images of conventional cells and NPP cells at different P_{RF} under coincident light injection conditions.

with the $\text{Al}_2\text{O}_3/\text{SiN}_x$ stacked films. The average τ_{eff} (2667 μs) and the maximum τ_{eff} (5124 μs) of symmetric lifetime samples at $\Delta n = 1 \times 10^{15}$ cm⁻³ confirm its excellent surface passivation capability. And this

stacked passivated layer was applied in all solar cells at different P_{RF} . Fig. 5b and c shows the evolutions of injection-dependent τ_{eff} and J_0 of cell-like precursors at different P_{RF} , respectively. When the P_{RF} increases

from 100 to 600 W, the average of τ_{eff} at $\Delta n = 1 \times 10^{15} \text{ cm}^{-3}$ increases from 548 to 682 μs , and the extracted J_0 decreases from 50.7 to 44.5 fA/cm^2 , which suggest that higher P_{RF} can adequately improve the passivation quality of NPP structures.

As described above, the feature sizes and morphologies of NPP structures affected by different P_{RF} have an effect on the boron emitter doping concentration and the interface defect state density, which ultimately determines the amount of emitter Auger recombination ($J_{0e, \text{Auger}}$) and surface SRH recombination ($J_{0e, \text{surface}}$) [41], respectively. Therefore, analyzing the occupation ratio of different recombination channels in NPP emitters can provide guidance for optimizing the preparation process of NPP solar cells. Based on the measured ECV profiles and J_0 extraction values, we disassemble the J_{0e} of NPP emitters and conventional micron-pyramid emitters into $J_{0e, \text{Auger}}$ and $J_{0e, \text{surface}}$ using ENDA 2 software [42], as shown in Fig. 5e. Note that the recombination channels of radiative (band-to-band) recombination and bulk SRH recombination were not plotted in Fig. 5e because they accounted for too little. On the one hand, the $J_{0e, \text{surface}}$ of NPP emitters ($21.8\text{--}23.6 \text{ fA/cm}^2$) at different P_{RF} have little difference and can be comparable to that of micron-pyramid emitter (20.1 fA/cm^2), which confirms the excellent surface defect passivation of the $\text{Al}_2\text{O}_3/\text{SiN}_x$ stacked layer on NPP textures. Among them, the lowest average $J_{0e, \text{surface}}$ of NPP emitter was obtained at the P_{RF} of 600 W, about 21.8 fA/cm^2 , indicating the benefit of larger feature sizes and smoother surface for surface passivation. As shown in Fig. 5d, the cross-sectional SEM image reflects the good conformality of the stacked passivation layer, which is essential for surface passivation on NPP structure. On the other hand, due to the heavy doping effect of nanostructures, the average $J_{0e, \text{Auger}}$ of NPP emitters ($14.9\text{--}19.6 \text{ fA/cm}^2$) at different P_{RF} are 99%–161% larger than that of micron-pyramid emitters (7.5 fA/cm^2). Meanwhile, when the P_{RF} increases from 100 to 600 W, the $J_{0e, \text{Auger}}$ of NPP emitters decreases from 19.6 to 14.9 fA/cm^2 , a drop of 24%, suggesting that the reduction of boron dopant caused by larger feature sizes effectively suppresses $J_{0e, \text{Auger}}$ as expected.

In summary, the difference of emitter passivation between NPP cells and micron-pyramid cells is mainly reflected in $J_{0e, \text{Auger}}$. At the same time, the $J_{0e, \text{surface}}$ over 20 fA/cm^2 still dominates the J_{0e} of NPP cells. Therefore, preparing the selective emitter, optimizing the boron diffusion process, and adjusting passivation technique to match NPP structures are the following research directions. Fig. 5f shows the PL luminescence intensity images of NPP cells at different P_{RF} before screen printing. The color difference of PL images characterizes local passivation in detail, and the PL mean values reflect global passivation quality. The positive relevant relationship between the PL mean value and the P_{RF} is coincident with passivation parameters measured by WCT-120.

3.3. Cell performance

To illustrate the broadband spectral absorption capability of NPP structures at the device level, Fig. 6a shows the EQE and reflectance spectra of NPP cells at different P_{RF} from 300 to 1200 nm, together with

conventional cells. Firstly, the reflectance of NPP cells in the short wavelength range of 300–450 nm is significantly lower than conventional cells, attributed to the formation of an EML as mentioned above. Secondly, the EQE of NPP cells in the short wavelength of 300–500 nm and medium-long wavelength of 700–1000 nm is higher than conventional cells, showing excellent broadband spectral response capability, beneficial to improving the J_{ph} of solar cells. Unlike silicon wafer, the non-trivial transport and recombination losses of incident light in NPP cells are more complicated. Based on the optical loss model proposed by Bertrand et al. [43] and the measured EQE and reflectance data, the various optical loss paths were quantified, as shown in Fig. 6b. Concerning the front-side reflection loss, NPP cells ($0.79\text{--}0.85 \text{ mA/cm}^2$) exhibits an improvement above 0.4 mA/cm^2 than conventional cells, corresponding to the results of EQE and reflectance in Fig. 6a, which confirms the strong antireflection capability of NPP structures. In addition, Fig. 6b reveals that the poly-Si/SiN_x parasitic absorption accounts for a large proportion of optical loss of a TOPCon cells. This can be reduced by reducing polysilicon thickness, but not completely eliminated. For NPP TOPCon solar cells, a higher light trapping at longer wavelengths helps to mitigate the parasitic light absorption in polysilicon layer. Hence, forming NPP textures could give us more flexibility with the thickness of the polysilicon layer.

The average current-voltage ($I\text{-}V$) electrical parameters of NPP cells are summed up in Table 2, together with conventional cells. The average V_{oc} of NPP cell at the P_{RF} of 600 W is more than 1–2 mV higher than those at the P_{RF} of 100 W and 300 W, which reveals passivation gains from larger feature sizes and smoother surface. The average J_{sc} of all NPP cells is greater than 41.43 mA/cm^2 , almost 2.8 mA/cm^2 higher than that of conventional cells (41.15 mA/cm^2), demonstrating the strong light-trapping capability of NPP structures on front surface. Furthermore, the average FF of NPP cells ($>81.55\%$) is above 0.31% higher than that of conventional cells (81.24%) due to the lower metal-silicon contact resistivity (ρ_c) formed by the heavy doping effect by NPP structures. The FF of NPP cells increases from 81.55% to 81.69% when the P_{RF} increases from 100 to 600 W because of the higher passivation quality at higher P_{RF} [44]. Altogether, the NPP cells at the P_{RF} of 600 W showed the highest average PCE (23.55%) compared with that of 100 W (23.48%), 300 W (23.45%) and conventional cells (23.37%). The high PCE of NPP cells at the P_{RF} of 600 W is derived from the appropriate surface morphology and feature size, which realizes a tradeoff between optical gain and recombination loss associated with NPP structures, that

Table 2

The average $I\text{-}V$ parameters of NPP cells at different P_{RF} and conventional cells, including PCE, V_{oc} , J_{sc} , FF and ρ_c .

RIE P_{RF} (W)	V_{oc} (mV)	J_{sc} (mA/cm^2)	FF (%)	PCE (%)	ρ_c ($\text{m}\Omega/\text{cm}^2$)
0	699.0	41.15	81.24	23.37	1.10
100	694.0	41.43	81.55	23.45	0.41
300	694.6	41.43	81.60	23.48	0.56
600	695.6	41.44	81.69	23.55	0.59

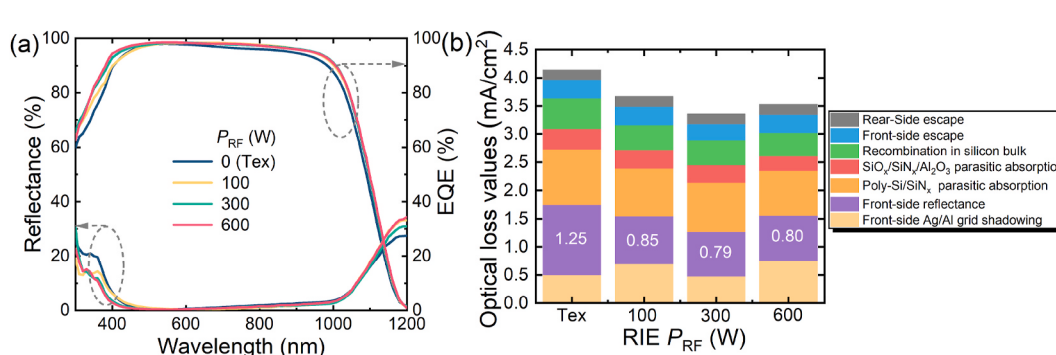


Fig. 6. (a) The EQE and reflectance spectra as a function of wavelength. (b) The optical loss path analysis of NPP cells at different P_{RF} and conventional cells.

is, it maintains the broadband spectral response capability and inhibits the severe Auger recombination and surface recombination as much as possible. A champion NPP cell was obtained on a full 252.02 cm² wafer area at the P_{RF} of 600 W, reaching a V_{oc} of 700.0 mV, an FF of 81.86%, an J_{sc} of 41.51 mA/cm², and a front PCE of 23.79%.

3.4. Wide-angle antireflection property

The angle dependence of spectral response capability of solar cells directly affects the total power generation of photovoltaic modules in all-weather working conditions when photovoltaic modules with fixed installation angle receive sunlight from different angles for one day due to the earth rotation. Here, the NPP cells at the P_{RF} of 600 W are selected to illustrate high-efficiency solar spectrum absorption performance for a wide θ because they exhibit better photoelectric properties. Fig. 7a and b shows the EQE spectra of NPP cells and conventional cells with increasing θ from 0° to 70°, respectively. The EQE spectra of NPP cells decreases slowly with increasing θ , which benefits from spectral response independent of the direction of incoming light that EML brings [6]. Differently, the EQE spectra of conventional cells drop dramatically with increasing θ , showing a strong angle sensitivity. This is because the micron-pyramids and anti-reflectance layers was mainly optimized and designed for reducing optical reflection in normal incident light. Fig. 7c shows the relative change in J_{sc} of NPP cells and conventional cells versus normal illumination as a function of θ . When the θ is less than 20°, changes in J_{sc} between NPP cells and conventional cells are almost overlapped. When the θ is increasing to 70°, changes in J_{sc} of NPP cells are under 4.5%, whereas conventional cells lose up to 7.4% in the same condition, which fully demonstrates the superior light-trapping capability of NPP cells over broad θ . During working in the outdoor environment, it is significant that NPP cells can generate higher total power and energy than conventional cells.

4. Conclusions

In summary, we have successfully demonstrated the high-efficiency NPP bifacial TOPCon solar cell with the highest PCE of 23.79% by integrating the RIE b-Si technique into industrial solar cell production. In this work, to ascertain the appropriate feature sizes and surface morphologies, we have systematically studied and analyzed the effects of different P_{RF} on photoelectric properties of NPP cells. Meanwhile, to further suppress a large amount of surface recombination and Auger recombination originated from NPP structures, the optimized boron diffusion process and high-quality stacked Al₂O₃/SiN_x layers were discussed. As a result, the larger subwavelength size of nanopores (~270 nm) and nanogrooves (~470 nm), and smoother surface were formed at the P_{RF} of 600 W, which notably promotes the emitter passivation quality ($J_{0e} \leq 36.7$ fA/cm²) while maintaining the strong light-trapping capability ($J_{sc} \geq 41.44$ mA/cm²). Besides, the EQE spectra results for several θ show that the relative changes in J_{sc} of NPP cells are under 4.5% for a wide θ up to 70°, exhibiting excellent wide-angle absorption capability and great application potential. This work should pave the way for the RIE technique in high-efficiency industrial TOPCon solar cells.

CRedit authorship contribution statement

Cheng Chen: Conceptualization, Methodology. **Cui Liu:** Visualization. **Jia Chen:** Investigation, Resources. **Zhifeng Liu:** Funding acquisition. **Xiao Yuan:** Project administration, Supervision. **Hongbo Li:** Supervision.

Declaration of competing interest

The authors declare that they have no known competing financial interests or personal relationships that could have appeared to influence

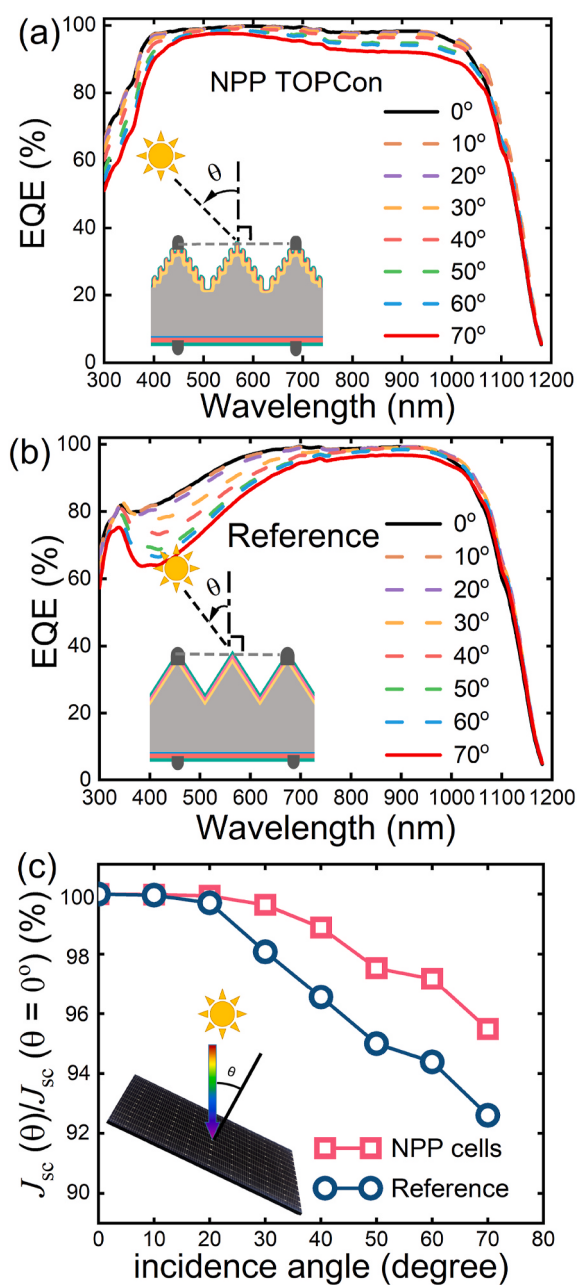


Fig. 7. The EQE spectra of (a) NPP cells and (b) conventional cells with increasing θ from 0° to 70°. (c) The ratio of J_{sc} at different θ (0° ~ 70°) to J_{sc} at the θ of 0° for both NPP cells and reference (conventional cells).

the work reported in this paper.

Acknowledgment

This work was supported by the National Key R&D Program of China (2018YFB1500300). We thank Changzhou Belight technology Co., Ltd for the help of the reactive ion etching process.

Appendix A. Supplementary data

Supplementary data to this article can be found online at <https://doi.org/10.1016/j.solmat.2022.111606>.

References

- [1] D. Chen, Y. Chen, Z. Wang, J. Gong, C. Liu, Y. Zou, Y. He, Y. Wang, L. Yuan, W. Lin, R. Xia, L. Yin, X. Zhang, G. Xu, Y. Yang, H. Shen, Z. Feng, P.P. Altermatt, P. J. Verlinden, 24.58% total area efficiency of screen-printed, large area industrial silicon solar cells with the tunnel oxide passivated contacts (i-TOPCon) design, *Sol. Energy Mater. Sol. Cells* 206 (2020), <https://doi.org/10.1016/j.solmat.2019.110258>.
- [2] J. Schmidt, R. Peibst, R. Brendel, Surface passivation of crystalline silicon solar cells: present and future, *Sol. Energy Mater. Sol. Cells* 187 (2018) 39–54, <https://doi.org/10.1016/j.solmat.2018.06.047>.
- [3] T.H. Fung, T.P. Pasanen, Y. Zhang, A. Soeriyadi, V. Vähäniemi, G. Scardera, D. Payne, H. Savin, M. Abbott, Improved emitter performance of RIE black silicon through the application of in-situ oxidation during POCl_3 diffusion, *Sol. Energy Mater. Sol. Cells* 210 (2020), <https://doi.org/10.1016/j.solmat.2020.110480>.
- [4] T.M. Mercier, T. Rahman, C. Krishnan, E. Khorani, P.J. Shaw, M.E. Pollard, S. A. Boden, P.G. Lagoudakis, M.D.B. Charlton, High symmetry nano-photonic quasi-crystals providing novel light management in silicon solar cells, *Nano Energy* 84 (2021), <https://doi.org/10.1016/j.nanoen.2021.105874>.
- [5] M.L. Brongersma, Y. Cui, S. Fan, Light management for photovoltaics using high-index nanostructures, *Nat. Mater.* 13 (5) (2014) 451–460, <https://doi.org/10.1038/nmat3921>.
- [6] X. Liu, P.R. Coxon, M. Peters, B. Hoex, J.M. Cole, D.J. Fray, Black silicon: fabrication methods, properties and solar energy applications, *Energy Environ. Sci.* 7 (10) (2014) 3223–3263, <https://doi.org/10.1039/c4ee01152j>.
- [7] M.A. Junutula, J. Heinonen, V. Vähäniemi, P. Repo, D. Valluru, H. Savin, Near-unity quantum efficiency of broadband black silicon photodiodes with an induced junction, *Nat. Photonics* 10 (12) (2016) 777–781, <https://doi.org/10.1038/nphoton.2016.226>.
- [8] M.G. Tanner, C.M. Natarajan, V.K. Pottapenjara, J.A. O'Connor, R.J. Warburton, R. H. Hadfield, B. Baek, S. Nam, S.N. Dorenbos, E.B. Urena, T. Zijlstra, T.M. Klapwijk, V. Zwiller, Enhanced telecom wavelength single-photon detection with NbTiN superconducting nanowires on oxidized silicon, *Appl. Phys. Lett.* 96 (22) (2010), <https://doi.org/10.1063/1.3428960>.
- [9] D.P. Tran, M.A. Winter, B. Wolfrum, R. Stockmann, C.T. Yang, M. Pourhassan-Moghaddam, A. Offenhausser, B. Thierry, Toward intraoperative detection of disseminated tumor cells in lymph nodes with silicon nanowire field effect transistors, *ACS Nano* 10 (2) (2016) 2357–2364, <https://doi.org/10.1021/acsnano.5b07136>.
- [10] H. Sai, H. Fujii, K. Arafune, Y. Ohshita, Y. Kanamori, H. Yugami, M. Yamaguchi, Wide-angle Antireflection effect of subwavelength structures for solar cells, *Jpn. J. Appl. Phys.* 46 (6A) (2007) 3333–3336, <https://doi.org/10.1143/jjap.46.3333>.
- [11] T. Rahman, R.S. Bonilla, A. Nawabjan, P.R. Wilshaw, S.A. Boden, Passivation of all-angle black surfaces for silicon solar cells, *Sol. Energy Mater. Sol. Cells* 160 (2017) 444–453, <https://doi.org/10.1016/j.solmat.2016.10.044>.
- [12] R.S. Davidsen, J. Ormstrup, M.L. Ommen, P.E. Larsen, M.S. Schmidt, A. Boisen, Ø. Nordseth, O. Hansen, Angle resolved characterization of nanostructured and conventionally textured silicon solar cells, *Sol. Energy Mater. Sol. Cells* 140 (2015) 134–140, <https://doi.org/10.1016/j.solmat.2015.04.001>.
- [13] Z.G. Huang, K. Gao, X.G. Wang, C. Xu, X.M. Song, L.X. Shi, Y. Zhang, B. Hoex, W. Z. Shen, Large-area MACE Si nano-inverted-pyramids for PERC solar cell application, *Sol. Energy* 188 (2019) 300–304, <https://doi.org/10.1016/j.solener.2019.06.015>.
- [14] J. Oh, H.C. Yuan, H.M. Branz, An 18.2%-efficient black-silicon solar cell achieved through control of carrier recombination in nanostructures, *Nat. Nanotechnol.* 7 (11) (2012) 743–748, <https://doi.org/10.1038/nano.2012.166>.
- [15] J. Benick, A. Richter, R. Müller, H. Hauser, F. Feldmann, P. Krenckel, S. Riepe, F. Schindler, M.C. Schubert, M. Hermle, A.W. Bett, S.W. Glunz, High-efficiency n-type HP mc silicon solar cells, *IEEE J. Photovolt.* 7 (5) (2017) 1171–1175, <https://doi.org/10.1109/jphotov.2017.2714139>.
- [16] Q. Wang, W. Zhou, Direct fabrication of cone array microstructure on monocrystalline silicon surface by femtosecond laser texturing, *Opt. Mater.* 72 (2017) 508–512, <https://doi.org/10.1016/j.optmat.2017.06.046>.
- [17] B.K. Nayak, V.V. Iyengar, M.C. Gupta, Efficient light trapping in silicon solar cells by ultrafast-laser-induced self-assembled micro/nano structures, *Prog. Photovoltaics.* 19 (6) (2011) 631–639, <https://doi.org/10.1002/pip.1067>.
- [18] T.P. Pasanen, H.S. Laine, V. Vahanissi, J. Schon, H. Savin, Black silicon significantly enhances phosphorus diffusion gettering, *Sci. Rep.* 8 (1) (2018) 1991, <https://doi.org/10.1038/s41598-018-20494-y>.
- [19] H. Savin, P. Repo, G. von Gastrow, P. Ortega, E. Calle, M. Garin, R. Alcubilla, Black silicon solar cells with interdigitated back-contacts achieve 22.1% efficiency, *Nat. Nanotechnol.* 10 (7) (2015) 624–628, <https://doi.org/10.1038/nano.2015.89>.
- [20] X. Jia, C. Zhou, W. Wang, Optimization of the surface structure on black silicon for surface passivation, *Nanoscale Res. Lett.* 12 (1) (2017) 193, <https://doi.org/10.1186/s11671-017-1910-6>.
- [21] F. Wu, H. Lin, Z. Yang, M. Liao, Z. Wang, Z. Li, P. Gao, J. Ye, W. Shen, Suppression of surface and Auger recombination by formation and control of radial junction in silicon microwire solar cells, *Nano Energy* 58 (2019) 817–824, <https://doi.org/10.1016/j.nanoen.2019.02.021>.
- [22] C. Modanese, H. Laine, T. Pasanen, H. Savin, J. Pearce, Economic advantages of dry-etched black silicon in passivated emitter rear cell (PERC) photovoltaic manufacturing, *Energies* 11 (9) (2018), <https://doi.org/10.3390/en11092337>.
- [23] M.L. Addonizio, A. Antoniaia, L. Fusco, Plasma etched c-Si wafer with proper pyramid-like nanostructures for photovoltaic applications, *Appl. Surf. Sci.* 467–468 (2019) 143–150, <https://doi.org/10.1016/j.apsusc.2018.10.078>.
- [24] J. Yoo, Reactive ion etching (RIE) technique for application in crystalline silicon solar cells, *Sol. Energy* 84 (4) (2010) 730–734, <https://doi.org/10.1016/j.solener.2010.01.031>.
- [25] K. Lee, I. Hwang, N. Kim, D. Choi, H.D. Um, S. Kim, K. Seo, 17.6%-Efficient radial junction solar cells using silicon nano/micro hybrid structures, *Nanoscale* 8 (30) (2016) 14473–14479, <https://doi.org/10.1039/c6nr04611h>.
- [26] G. von Gastrow, P. Ortega, R. Alcubilla, S. Husein, T. Nietzold, M. Bertoni, H. Savin, Recombination processes in passivated boron-implanted black silicon emitters, *J. Appl. Phys.* 121 (18) (2017), <https://doi.org/10.1063/1.4983297>.
- [27] M.J.d. Boer, J.G.E. Gardiners, H.V. Jansen, E. Smulders, M. Gilde, R. Roelofs, J. N. Sasserath, M. Elwenspoek, Guidelines for etching silicon MEMS structures using fluorine high-density plasmas at cryogenic temperatures, *J. Microelectromech. Syst.* 11 (4) (2002) 385–401, <https://doi.org/10.1109/JMEMS.2002.800928>.
- [28] H.V. Jansen, M.J. de Boer, S. Unnikrishnan, M.C. Louwerse, M.C. Elwenspoek, Black silicon method: X. A review on high speed and selective plasma etching of silicon with profile control: an in-depth comparison between Bosch and cryostat DRIE processes as a roadmap to next generation equipment, *J. Micromech. Microeng.* 19 (3) (2009), <https://doi.org/10.1088/0960-1317/19/3/033001>.
- [29] S. Kalem, P. Werner, O. Arthursson, V. Talalaev, B. Nilsson, M. Hagberg, H. Frederiksen, U. Sodervall, Black silicon with high density and high aspect ratio nanowhiskers, *Nanotechnology* 22 (23) (2011) 235307, <https://doi.org/10.1088/0957-4484/22/23/235307>.
- [30] G. Kumaravelu, M.M. Alkaabi, A. Bittar, Surface texturing for silicon solar cells using reactive ion etching technique, in: 29th IEEE Photovolt. Specialists Conf., 2002, pp. 258–261, <https://doi.org/10.1109/pvsc.2002.1190507>, 2002.
- [31] R. Dussart, T. Tillicher, P. Lefacheux, M. Boufniichel, Plasma cryogenic etching of silicon: from the early days to today's advanced technologies, *J. Phys. D Appl. Phys.* 47 (12) (2014), <https://doi.org/10.1088/0022-3727/47/12/123001>.
- [32] H.M. Branz, V.E. Yost, S. Ward, K.M. Jones, B. To, P. Stradins, Nanostructured black silicon and the optical reflectance of graded-density surfaces, *Appl. Phys. Lett.* 94 (23) (2009), <https://doi.org/10.1063/1.3152244>.
- [33] S. Zhong, Z. Huang, X. Lin, Y. Zeng, Y. Ma, W. Shen, High-efficiency nanostructured silicon solar cells on a large scale realized through the suppression of recombination channels, *Adv. Mater.* 27 (3) (2015) 555–561, <https://doi.org/10.1002/adma.201401553>.
- [34] V. Torres-Costa, F. Agulló-Rueda, R.J. Martín-Palma, J.M. Martínez-Duart, Porous silicon optical devices for sensing applications, *Opt. Mater.* 27 (5) (2005) 1084–1087, <https://doi.org/10.1016/j.optmat.2004.08.068>.
- [35] H.-J. Kim, Y.-Y. Kim, K.-W. Lee, Multiparametric sensor based on DBR porous silicon for detection of ethanol gas, *Curr. Appl. Phys.* 10 (1) (2010) 181–183, <https://doi.org/10.1016/j.cap.2009.04.020>.
- [36] Q. Yang, X.A. Zhang, A. Bagal, W. Guo, C.H. Chang, Antireflection effects at nanostructured material interfaces and the suppression of thin-film interference, *Nanotechnology* 24 (23) (2013) 235202, <https://doi.org/10.1088/0957-4484/24/23/235202>.
- [37] J. Hirsch, M. Gaudig, N. Bernhard, D. Lausch, Optoelectronic properties of Black-Silicon generated through inductively coupled plasma (ICP) processing for crystalline silicon solar cells, *Appl. Surf. Sci.* 374 (2016) 252–256, <https://doi.org/10.1016/j.apsusc.2015.11.241>.
- [38] V.D. Mihailitchi, H. Chu, J. Lossen, R. Kopecek, Surface passivation of boron diffused junctions by borosilicate glass and in situ grown silicon dioxide interface layer, in: 2017 44th IEEE Photovolt. Specialist Conf., 2017, pp. 1222–1227, <https://doi.org/10.1109/pvsc.2017.8366702>.
- [39] H. Wagner, S. Steingrube, B. Wolpensinger, A. Dastgheib-Shirazi, R. Chen, S. T. Dunham, P.P. Altermatt, Analyzing emitter dopant inhomogeneities at textured Si surfaces by using 3D process and device simulations in combination with SEM imaging, in: 2012 38th IEEE Photovolt. Specialists Conf., 2012, pp. 313–316, <https://doi.org/10.1109/PVSC.2012.6317625>.
- [40] G. Dingemans, W.M.M. Kessels, Status and prospects of Al_2O_3 -based surface passivation schemes for silicon solar cells, *J. Vac. Sci. Technol.* 30 (4) (2012), <https://doi.org/10.1116/1.4728205>.
- [41] A. Kimmerle, J. Greulich, A. Wolf, Carrier-diffusion corrected J_0 -analysis of charge carrier lifetime measurements for increased consistency, *Sol. Energy Mater. Sol. Cells* 142 (2015) 116–122, <https://doi.org/10.1016/j.solmat.2015.06.043>.
- [42] K.R. McIntosh, P.P. Altermatt, T.J. Ratcliff, F. Kean Chern, L.E. Black, S.C. Baker-Finch, M.D. Abbott, An examination of three common assumptions used to simulate recombination in heavily doped silicon, in: 28th Eur. Photovol. Sol. Energy Conf. Exhib., 2013, pp. 1672–1679, <https://doi.org/10.4229/28thEUPVSEC2013-2CV.4.9>.
- [43] B. Paviet-Salomon, A. Tomasi, A. Descoedres, L. Barraud, S. Nicolay, M. Despeisse, S.D. Wolf, C. Ballif, Back-Contacted silicon heterojunction solar cells: optical-loss analysis and mitigation, *IEEE J. Photovolt.* 5 (5) (2015) 1293–1303, <https://doi.org/10.1109/jphotov.2015.2438641>.
- [44] A. Richter, R. Müller, J. Benick, F. Feldmann, B. Steinhauser, C. Reichel, A. Fell, M. Bivour, M. Hermle, S.W. Glunz, Design rules for high-efficiency both-sides-contacted silicon solar cells with balanced charge carrier transport and recombination losses, *Nat. Energy* 6 (4) (2021) 429–438, <https://doi.org/10.1038/s41560-021-00805-w>.